Mechatronics 92 (2023) 102981

Contents lists available at ScienceDirect

Mechatronics

journal homepage: www.elsevier.com/locate/mechatronics

Output feedback control design for quadrotor using recursive least square dynamic inversion☆

Seongwon Lee [a], Joowhan Seo [b], Joonho Lee [c,1], Connor Boss [d], Jongeun Choi [e,*]

[a] Department of Mechanical Science and Engineering, University of Illinois Urbana-Champaign, 201 N Goodwin Ave, Champaign, IL 61801, USA
[b] Department of Mechanical Engineering, University of California, 2521 Hearst Ave, Berkeley, CA 94709, USA
[c] Guidance, Navigation, Controls and Autonomy, Boeing Research and Technology, Everett, WA 98204, USA
[d] JHU Applied Physics Laboratory, 11100 Johns Hopkins Rd, Laurel, MD 20723, USA
[e] School of Mechanical Engineering, Yonsei University, 50 Yonsei Ro, Seodaemun Gu, Seoul 03722, Republic of Korea

ARTICLE INFO

Keywords:
Quadrotor
UAVs
Nonlinear controls
Underactuated mechanical systems
Dynamic inversion
Recursive least square
Extended high-gain observers

ABSTRACT

This paper proposes a new trajectory tracking output feedback control design for quadrotor unmanned aerial vehicles (UAVs) to manage stable flight in the outdoor environment with strong uncertainties, i.e., wind gusts. The controller is designed to handle unmeasured system states, disturbances, and uncertainties. Extended High-Gain Observers (EHGO) are employed to estimate the unmeasured system states and disturbances. A newly designed controller, namely Recursive Least Square with Dynamic Inversion (RLS-DI) controller, determines the coefficient of the input Jacobian to deal with the system uncertainties present in the input Jacobian. To deal with the underactuation characteristic inherited in the quadrotor, the controller and plant dynamics are separated into multi-time-scale structures. The stability of the closed-loop system is analyzed using the singular perturbation method. Through numerical simulations and outdoor experiments under the wind gust, the effectiveness of the proposed control algorithm is verified.

1. Introduction

Quadrotor control is challenging because the dynamics have intrinsic unstable features [1]. Furthermore, quadrotors are influenced by external disturbances, which result in additional uncertainties for the control design. Since quadrotors are used in a wide range of applications, it is essential to create a robust control system under external uncertainties in order to ensure the stable flight of the quadrotor. In this paper, we present the output feedback controller that tracks trajectories (x, y, z, and yaw) under uncertainties utilizing the recursive least square combined with the dynamic inversion method on top of the multi-time-scale structure.

Backstepping and sliding mode control (SMC) methods are extensively used to add robustness to nonlinear control designs of the quadrotor under uncertainties. In [2], SMCs were designed to cancel the uncertainties in a quadrotor system and to address the underactuation by dividing states into indirect and direct states. In [3], a continuous sliding-mode control (CSMC) method was introduced to achieve strong robustness to various disturbances on the quadrotor. Based on the disturbance observer, the CSMC approach is used to deal with both matched and mismatched uncertainty in [4]. An adaptive backstepping scheme was used to manage constant parameter uncertainties which may be present in the quadrotor dynamics [5]. In [6], the finite-time backstepping approach is introduced to improve convergence properties near the trim point. [7] proposed a control method that circumvents both underactuation issues and cascade constraints caused by the cascade structure. This method recursively stabilizes tracking errors by incorporating the SMC and dynamic surface control approaches into a backstepping-like framework. In [8], the authors present an accurate trajectory tracking controller that utilizes the sliding-mode error surfaces in rotation dynamics. This method allows two heterogeneous systems under the complex unknowns to develop independently in the translation–rotation cascade manners.

To overcome the external disturbances and unmeasured states, various types of controllers and observers are utilized. In [9], the integral of the signum of the error-based controller is utilized for the inner-loop subsystem, and the immersion and invariance method is utilized for the

☆ This paper was recommended for publication by Associate Editor Weichao Sun.

* Corresponding author.
E-mail addresses: sl148@illinois.edu (S. Lee), joohwan_seo@berkeley.edu (J. Seo), joonho.lee5@boeing.com (J. Lee), connor.boss@jhuapl.edu (C. Boss), jongeunchoi@yonsei.ac.kr (J. Choi).

[1] **Disclaimer:** The views and opinions expressed in this paper are those of the authors and do not necessarily reflect the official policy or position of The Boeing Company.

https://doi.org/10.1016/j.mechatronics.2023.102981
Received 24 June 2022; Received in revised form 27 January 2023; Accepted 30 March 2023
Available online 10 April 2023

outer-loop subsystem. In [10], a nonlinear H_∞ control scheme was used to stabilize the rotational dynamics while a model predictive control (MPC) scheme was utilized to track trajectories in the translational dynamics under state feedback. In [11], a dynamic inversion and L_1 adaptive control were combined to deal with unmeasured states, uncertainties, and input delay. [12] proposed a disturbance observer with the backstepping approach to achieve the disturbance attenuation control of the quadrotor UAV. The high-gain observer-based approach with FL control is employed to compensate for actuator and sensor faults in [13]. Robust controllers for an uncertain payload were designed using SMC and backstepping control in [14,15], respectively.

Neural networks (NNs) based UAVs controllers are extensively studied. In [16], NNs are used for the controller and observers to learn quadrotor dynamics in an online manner, including uncertain nonlinear terms such as aerodynamic friction. To estimate the disturbances, [17] uses NNs with a feedback-linearization (FL) method for precise landing and takeoff by approximating disturbances and incorporating them into an exponentially stabilizing controller. In [18], a geometric adaptive controller was augmented with NNs to mitigate unknown disturbances. [19] proposed an adaptive neural network-based trajectory tracking controller that is robust against parametric uncertainties of the inner loop. Without knowing the parameters of the quadrotor and the inaccessible inner loop controller, the controller was able to accurately track the trajectories.

One of the drawbacks of the aforementioned approaches is that they assume approximated dynamics, i.e., approximated inputs Jacobians. Moreover, these schemes assume a fixed input Jacobian matrix, which is inevitably vulnerable to uncertainties in the input Jacobian matrix. These uncertainties may raise a stability issue when the controller is implemented in the quadrotor hardware and tested in the environment under highly uncertain disturbances. To address this problem, we propose a new control strategy that is robust against plant model uncertainties and external disturbances. We employ a multi-time-scale structure to overcome the underactuation present in quadrotors and achieve it by stratifying high feedback gains of the quadrotor's controllers and dynamics. This multi-time-scale structure is explained in detail in Section 3. On top of this, the dynamic inversion (DI) [20–22] is utilized to directly deal with the inputs Jacobian. In contrast to the DI method proposed in [21,22], we combine the Recursive Least Square (RLS) method with the DI method to allow further robustness to the uncertainties in the input Jacobian. The RLS recursively computes the error between the reference trajectories and current states and reflects this error into the input Jacobians, which governs the control input's update rule of the DI. In addition, the extended high-gain observer (EHGO) is employed to estimate the model uncertainties, unmeasured system states, and external disturbances. The main contributions are as follows:

1. We design a novel output feedback controller using DI, based on the RLS method (RLS-DI), to deal with uncertain input coefficients. The EHGO is combined with the newly designed RLS-DI (EHGO-RLS-DI) to estimate the controller's unmeasured system states and uncertainties.
2. The stability of the controller is analyzed using the singular perturbation method [23], which guarantees the stability on the closed-loop system.
3. To show the outperformance of our proposed scheme, both the perturbed input Jacobian of the FL method combined with the EHGO [24] (EHGO-FL) and the disturbance observer-based CSMC (DOB-CSMC) control strategy are considered in a benchmark study. Under the same perturbation, the EHGO-RLS-DI outperforms the EHGO-FL and the DOB-CSMC.
4. The proposed controller is discretized to perform the outdoor hardware experiments in the presence of wind gusts. The results shows that the EHGO-RLS-DI outperformed the EHGO-FL.

This paper is organized as follows. In Section 2, the dynamics and assumptions for the quadrotor are introduced. The output feedback control in the presence of uncertainties is presented in Section 3. The closed-loop system stability analysis for the proposed controller is shown in Section 4. Section 5 presents the numerical simulation result of the proposed controller and compares it with benchmark controllers. In Section 6, hardware implementation of the proposed control demonstrates that the proposed control design is effective for outdoor flight. Concluding remarks and future works are given in Section 7.

2. Quadrotor dynamic model

Using the body coordinate frame given by the Newton–Euler equation, the equations of motion for quadrotors in [25] are

$$\begin{bmatrix} M & 0_{3\times3} \\ 0_{3\times3} & I \end{bmatrix} \begin{bmatrix} \dot{v}^b \\ \dot{\omega}^b \end{bmatrix} + \begin{bmatrix} \omega^b \times m v^b \\ \omega^b \times I\omega^b \end{bmatrix} = \begin{bmatrix} f^b \\ \tau^b \end{bmatrix}, \tag{1}$$

where $M = \mathrm{diag}(m,\ m,\ m) \in \mathbb{R}^{3\times3}$ is a mass matrix with $m > 0$. The inertia matrix is $I = \mathrm{diag}[I_{xx}, I_{yy}, I_{zz}] \in \mathbb{R}^{3\times3}$, and I_{xx}, I_{yy}, and I_{zz} are principle moments of inertia along the body-fixed x-, y-, and z-axes, respectively. The velocity vector is $v^b = [v_x,\ v_y,\ v_z]^T \in \mathbb{R}^3$ where the subscripts indicate each inertial axes. The angular velocity vector is $\omega^b = [\omega_1,\ \omega_2,\ \omega_3]^T \in \mathbb{R}^3$ where ω_1, ω_2, and ω_3 are the angular velocities along the body-fixed x-, y-, and z-axes, respectively. The body force is $f^b \in \mathbb{R}^3$, defined as

$$f^b = [0,\ 0,\ u_1]^T + R[0,\ 0,\ mg]^T,$$

$$R = \begin{bmatrix} c\theta c\psi & (s\phi s\theta c\psi - c\theta s\psi) & (c\phi s\theta c\psi + s\phi s\psi) \\ c\theta s\psi & (s\phi s\theta s\psi + c\phi c\psi) & (c\phi s\theta s\psi - s\phi c\psi) \\ -s\theta & s\phi c\theta & c\phi c\theta \end{bmatrix},$$

where $c(\cdot) = \cos(\cdot)$, $s(\cdot) = \sin(\cdot)$, and ϕ, θ, and ψ are the roll, pitch, and yaw angles, respectively. The translational control input $u_1 \in \mathbb{R}$ is a force applied along the body-fixed z-axes. The rotational control inputs are u_2, u_3, and u_4, and the torque vector $\tau^b = [u_2,\ u_3,\ u_4]^T \in \mathbb{R}^3$ is applied to the center of mass in the body-fixed coordinate frame. The Euler angles $\Theta_b = [\phi,\ \theta,\ \psi]^T$ have the following relation with ω^b

$$\dot{\Theta}_b = \Psi(\Theta_b)\omega^b, \quad \Psi = \begin{bmatrix} 1 & s\phi t\theta & c\phi t\theta \\ 0 & c\phi & -s\phi \\ 0 & s\phi/c\theta & c\phi/c\theta \end{bmatrix},$$

where $t(\cdot) = \tan(\cdot)$. Defining the state variables

$$X = [X_x^T,\ X_y^T,\ X_z^T]^T, \quad X_x = [x_1,\ x_2]^T = [x,\ \dot{x}]^T,$$
$$X_y = [y_1,\ y_2]^T = [y,\ \dot{y}]^T, \quad X_z = [z_1,\ z_2]^T = [z,\ \dot{z}]^T,$$
$$\Theta = [\Theta_\phi^T,\ \Theta_\theta^T,\ \Theta_\psi^T]^T, \quad \Theta_\phi = [\phi_1,\ \phi_2]^T = [\phi,\ \dot{\phi}]^T,$$
$$\Theta_\theta = [\theta_1,\ \theta_2]^T = [\theta,\ \dot{\theta}]^T, \quad \Theta_\psi = [\psi_1,\ \psi_2]^T = [\psi,\ \dot{\psi}]^T,$$

the state space equations for (1) can be written as

$$\begin{aligned} \dot{X} &= AX + BF_X, \quad y_x = CX, \\ \dot{\Theta} &= A\Theta + BF_\Theta, \quad y_\theta = C\Theta, \end{aligned} \tag{2}$$

where $X \in D_X \subset \mathbb{R}^6$ and $\Theta \in D_\Theta \subset \mathbb{R}^6$, and D_X and D_Θ bounded. We define $D_\Theta = D_{\Theta_1} \times D_{\Theta_2}$ where $\Theta_1 = [\phi_1,\ \theta_1,\ \psi_1]^T \in D_{\Theta_1} \subset \mathbb{R}^3$ and $\Theta_2 = [\phi_2,\ \theta_2,\ \psi_2]^T \in D_{\Theta_2} \subset \mathbb{R}^3$ where $D_{\Theta_1} = D_{\phi_s} \times D_{\Theta_s} \times D_{\psi_s}$ with $D_{\phi_s} = \{-\pi/2 < \phi_1 < \pi/2\}$, $D_{\Theta_s} = \{-\pi/2 < \theta_1 < \pi/2\}$, and $D_{\psi_s} = \{-\pi/2 < \psi_1 < \pi/2\}$. The matrices are $A = \text{block diag}[A_1, A_1, A_1]$, $B = \text{block diag}[B_1, B_1, B_1]$, and $C = \text{block diag}[C_1, C_1, C_1]$ where

$$A_1 = \begin{bmatrix} 0 & 1 \\ 0 & 0 \end{bmatrix}, \quad B_1 = \begin{bmatrix} 0 \\ 1 \end{bmatrix}, \quad C_1 = [1, 0],$$

$F_X = \left[F_x, F_y, F_z\right]^T$ and $F_\Theta = \left[F_\phi, F_\theta, F_\psi\right]^T$ are given by

$$F_X = -\frac{1}{m} \begin{bmatrix} (c\phi_1 s\theta_1 c\psi_1 + s\phi_1 s\psi_1)u_1 \\ (c\phi_1 s\theta_1 s\psi_1 - s\phi_1 c\psi_1)u_1 \\ (c\phi_1 c\theta_1)u_1 \end{bmatrix} + \begin{bmatrix} 0 \\ 0 \\ g \end{bmatrix},$$

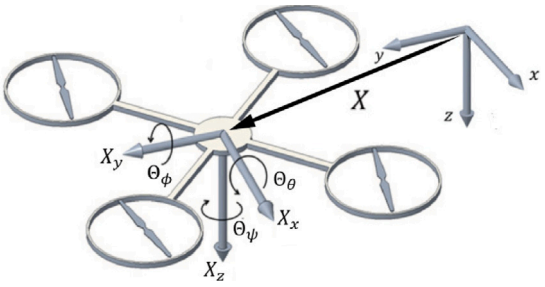

Fig. 1. Coordinates of a quadrotor.

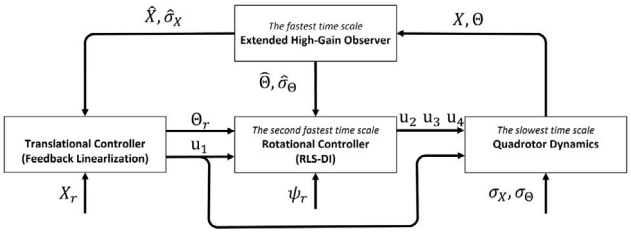

Fig. 2. The multi-time-scale structure of the proposed output feedback controller. The EHGO resides in the fastest time scale to provide estimates of states ($\hat{X}$ and $\hat{\Theta}$) and uncertainties ($\hat{\sigma}_X$ and $\hat{\sigma}_\Theta$). The translational controller (feedback linearization) receives the translational estimates ($\hat{X}$), uncertainties ($\hat{\sigma}_\Theta$), and reference trajectory (X_r) and then passes the rotational reference trajectory (Θ_r) to the rotational controller, which resides in the second fastest time scale. Next, the rotational controller (RLS-DI) receives the rotational reference (Θ_r) and translational input (u_1) and then passes control inputs (u_2, u_3, u_4) to the quadrotor dynamics, which resides in the slowest time scale. Lastly, the quadrotor dynamics under the translational and rotational uncertainties (σ_X and σ_Θ) takes in the control inputs (u_1, u_2, u_3, u_4) to track the given trajectories (X_r and ψ_r) and outputs the new states (X and Θ).

$$F_\Theta = F_{\Theta_1} + B_d \tau^b, \quad B_d = \Psi(\Theta_1) I^{-1},$$
$$F_{\Theta_1} = \dot{\Psi}(\Theta)\omega^b + \Psi(\Theta_1)[-I^{-1}\omega^b \times I\omega^b],$$

where $g = 9.81$ (m/s^2) is gravitational acceleration. The system equations of (2) in the presence of uncertainties are rewritten as

$$\dot{X} = AX + B[F_{X_n}(\Theta, u_1) + \sigma_X(t)],$$
$$\dot{\Theta} = A\Theta + B[F_{\Theta_n}(\Theta, U_R) + \sigma_\Theta(t)],$$

where $F_{X_n} = [F_{x_n}, F_{y_n}, F_{z_n}]^T$ and $F_{\Theta_n} = [F_{\phi_n}, F_{\theta_n}, F_{\psi_n}]^T$ are a nominal model of F_X and F_Θ, respectively, $U_R = [u_2, u_3, u_4]^T$ is the rotational control input, σ_X and σ_Θ are the translational and rotational disturbances, respectively (see Fig. 1).

Assumption 1. The functions $\sigma_X(t)$ and $\sigma_\Theta(t)$ are continuously differentiable and bounded as per the requirements of the EHGO.

There is a mapping that describes the relationship between the actuators and the control inputs u_i for $i = 1, \ldots, 4$ as follows.

$$u = \mathcal{F}(X, \Theta) + \mathcal{G}(X, \Theta, U)$$

where $\mathcal{F} \in D_F \subset \mathbb{R}^4$ and $\mathcal{G} \in D_G$ whose dimension is appropriate to U. The domains D_F and D_G are compact sets.

3. Control design in continuous time

In this section, an output feedback controller will be designed using a multi-time-scale structure. The illustration of the system's architecture is shown in Fig. 2. We utilized the multi-time-scale structure to overcome the underactuation, and it is achieved by stratifying gains of the quadrotor's plant dynamics, controllers, and observers. For example, the controller forces the rotational dynamics to be faster than the translational dynamics by employing a higher gain on the rotational dynamics than the translational dynamics. The fastest time scale is for the EHGO in order for the EHGO to readily provide estimates and uncertainties to the translational and rotational controller. The second fastest time scale is for the rotational controller, which receives the estimates from the EHGO, and outputs the rotational control inputs which to be used in the plant dynamics. The slowest time scale is for the quadrotor plant dynamics that updates the states according to the control inputs.

To adaptively update and handle the input Jacobian according to the uncertainties that exist in the input Jacobian, we utilize the DI with the RLS method. The RLS recursively computes the coefficient matrix of the input Jacobian, instead of using the fixed input Jacobian. Since the RLS recursively computes the tracking error rather than solely computing the current tracking error, the coefficient matrix is adaptively updated according to the combined tracking error, reflecting uncertainties presented in the input Jacobian. Note that our newly developed Recursive Least Square with Dynamic Inversion (RLS-DI) control method is for the rotational controller, while the translational controller is employed from FL method [26,27].

3.1. Extended high-gain observers

The EHGO estimates unmeasured states and uncertainties and utilizes high feedback gains to recover the peaking of the estimation and to guarantee the stability of the closed-loop system. Thus, to attenuate the effect of the disturbances, the EHGO in [24] is designed as

$$\begin{aligned}
\dot{\hat{X}} &= A\hat{X} + B[F_{X_n}(\hat{X}, u_1) + \hat{\sigma}_X(t)] + H_x(\varepsilon_3)(y_x - C\hat{X}),\\
\dot{\hat{\sigma}}_X &= H_{x_e}(y_x - C\hat{X}),\\
\dot{\hat{\Theta}} &= A\hat{\Theta} + B[F_{\Theta_n}(\hat{\Theta}, U_R) + \hat{\sigma}_\Theta(t)] + H_\theta(\varepsilon_3)(y_\theta - C\hat{\Theta}),\\
\dot{\hat{\sigma}}_\Theta &= H_{\theta_e}(y_\theta - C\hat{\Theta}),
\end{aligned} \tag{3}$$

where the estimates of X and Θ are $\hat{X} = [\hat{X}_x^T, \hat{X}_y^T, \hat{X}_z^T]^T$ and $\hat{\Theta} = [\hat{\Theta}_\phi^T, \hat{\Theta}_\theta^T, \hat{\Theta}_\psi^T]^T$, respectively. Furthermore, $\hat{X}_x = [\hat{x}_1, \hat{x}_2]^T$, $\hat{X}_y = [\hat{y}_1, \hat{y}_2]^T$, $\hat{X}_z = [\hat{z}_1, \hat{z}_2]^T$, $\hat{\Theta}_\phi = [\hat{\phi}_1, \hat{\phi}_2]^T$, $\hat{\Theta}_\theta = [\hat{\theta}_1, \hat{\theta}_2]^T$, $\hat{\Theta}_\psi = [\hat{\psi}_1, \hat{\psi}_2]^T$. The estimates of σ_X and σ_Θ are $\hat{\sigma}_X = [\hat{\sigma}_x, \hat{\sigma}_y, \hat{\sigma}_z]^T$ and $\hat{\sigma}_\Theta = [\hat{\sigma}_\phi, \hat{\sigma}_\theta, \hat{\sigma}_\psi]^T$, respectively. The observer gains, H_x, H_{x_e}, H_θ, and H_{θ_e} are defined as

$$\begin{aligned}
H_x &= \text{block diag}[H_{x_1}, H_{x_2}, H_{x_3}], \quad H_{x_i} = [\alpha_{i1}/\varepsilon_3, \alpha_{i2}/\varepsilon_3^2]^T,\\
H_{x_e} &= \text{diag}(\alpha_{x3}/\varepsilon_3^3,\ \alpha_{y3}/\varepsilon_3^3,\ \alpha_{z3}/\varepsilon_3^3), \quad i = x, y, z,\\
H_\theta &= \text{block diag}[H_{\theta_4}, H_{\theta_5}, H_{\theta_6}], \quad H_{\theta_j} = [\alpha_{j1}/\varepsilon_3\ \alpha_{j2}/\varepsilon_3^2]^T,\\
H_{\theta_e} &= \text{diag}(\alpha_{\phi 3}/\varepsilon_3^3,\ \alpha_{\theta 3}/\varepsilon_3^3,\ \alpha_{\psi 3}/\varepsilon_3^3), \quad j = \phi, \theta, \psi.
\end{aligned} \tag{4}$$

where gains $\alpha_{i,j}$ for $i = x, y, z, \phi, \theta, \psi$ and $j = 1, 2, 3$ are chosen such that the polynomials, $s^3 + \alpha_{i1}s^2 + \alpha_{i2}s + \alpha_{i3}$ for $i = x, y, z, \phi, \theta, \psi$, are Hurwitz. $0 < \varepsilon_3 < 1$ is a small positive constant.

3.2. Output feedback controller for rotational dynamics (RLS-DI)

The output feedback control for rotational dynamics is designed based on the estimates from the EHGO. Our RLS-DI is introduced to deal directly with the input Jacobian. In the DI method, the control inputs cannot be computed if the Jacobian matrix is calculated as singular due to the uncertain inputs in the controller. To avoid this issue, we define a sector condition as follows.

Assumption 2. There is a unique continuously differentiable function $U(t, \Theta, U_R, \phi_v, \theta_v)$ such that $U_R^* = U(t, \Theta, U_R, \phi_v, \theta_v)$ solves the equation

$$\mathbf{F}_\Theta = F_{\Theta_n}(t, \Theta, U_R^*) + \sigma_\Theta - f_{r_\Theta}(t, \Theta) = 0 \tag{5}$$

where F_{Θ_n} is a nominal model, and f_{r_Θ} is a reference vector. The derivative $\dot{U}_R^*$ is bounded on compact sets of Θ. Furthermore, there is

a known matrix K, such that the terms $F_{\Theta_n}+\sigma_\Theta - f_{r_\Theta}$ satisfy the sector condition

$$s_r{}^T K \mathbf{F}_\Theta \geq \beta s_r{}^T s_r \tag{6}$$

with $s_r = U_R - U_R^*$ and the positive constant $\beta > 0$.

Given the estimates from EHGO , the rotational controller utilizes RLS-DI as

$$\varepsilon_2 \dot{U}_R = -P^T \mathbf{F}_{\hat{\Theta}_s}, \quad U_R(0) = U_{R_0}, \tag{7}$$

$$\mathbf{F}_{\hat{\Theta}_s} = F_{\Theta_n} + \hat{\sigma}_\Theta - f_{r_{\hat{\Theta}}} = \begin{bmatrix} F_{\phi_n} + \hat{\sigma}_{\phi s} - f_{r_{\hat{\phi}}} \\ F_{\theta_n} + \hat{\sigma}_{\theta s} - f_{r_{\hat{\theta}}} \\ F_{\psi_n} + \hat{\sigma}_{\psi s} - f_{r_{\hat{\psi}}} \end{bmatrix}, \tag{8}$$

where P is a coefficient matrix with $\dot{P} = -P^T P$, $P(0) = P_0$, and ε_2 satisfies $0 < \varepsilon_3 \ll \varepsilon_2 < 1$ for the multi-time-scale separation. $\hat{\Theta}_s$ and $\hat{\sigma}_{\Theta s}$ are a saturated $\hat{\Theta}$ and $\hat{\sigma}_\Theta$, respectively. $U_R \in D_R \subset \mathbb{R}^3$, $P \in D_P \subset \mathbb{R}^{3\times 3}$ where D_R and D_P are bounded. Furthermore, the reference vector $f_{r_{\hat{\Theta}}}$, is given by

$$f_{r_{\hat{\Theta}}} = \begin{bmatrix} f_{r_{\hat{\phi}}} \\ f_{r_{\hat{\theta}}} \\ f_{r_{\hat{\psi}}} \end{bmatrix} = \begin{bmatrix} -k_{\phi_1}(\phi_1 - \phi_v) - k_{\phi_2}\hat{\phi}_{2s} \\ -k_{\theta_1}(\theta_1 - \theta_v) - k_{\theta_2}\hat{\theta}_{2s} \\ -k_{\psi_1}(\psi_1 - \psi_r) - k_{\psi_2}\hat{\psi}_{2s} \end{bmatrix}. \tag{9}$$

ϕ_v and θ_v are the trajectories given from the translational controller as (12), and ψ_r is a differentiable bounded reference. The control gains are

$$k_{\phi_1} = k_{\theta_1} = k_{\psi_1} = \frac{k_1}{\varepsilon_1^2}, \quad k_{\phi_2} = k_{\theta_2} = k_{\psi_2} = \frac{k_2}{\varepsilon_1}, \tag{10}$$

where k_1 and k_2 are chosen such that the polynomial $s^2 + k_2 s + k_1$ is Hurwitz. The small positive constant ε_1 is chosen to satisfy the multi-time-scale separation condition $0 < \varepsilon_3 \ll \varepsilon_2 \ll \varepsilon_1 < 1$, and to ensure a quick convergence of ϕ_1, θ_1, and ψ_1 to the trajectories ϕ_v, θ_v, and ψ_d, respectively. In (8) and (9), $\hat{\imath}_{2s}$ and $\hat{\sigma}_{is}$ for $i = \phi, \theta, \psi$ are

$$\hat{\imath}_{2s} = M_{\hat{\imath}_{2s}} \text{sat}\left(\frac{\hat{\imath}_{2s}}{M_{\hat{\imath}_{2s}}}\right), \quad \hat{\sigma}_{is} = M_{\hat{\sigma}_{is}} \text{sat}\left(\frac{\hat{\sigma}_{is}}{M_{\hat{\sigma}_{is}}}\right). \tag{11}$$

where the saturation operator sat(e) is defined as

$$\text{sat}(e) = \begin{cases} e, & \text{if} \quad |e| \leq 1, \\ \text{sign}(e), & \text{if} \quad |e| > 1. \end{cases}$$

The saturation levels, $M_{\hat{\imath}_{2s}}$ and $M_{\hat{\sigma}_{is}}$, are chosen so as not to be active under state feedback control.

3.3. Output feedback controller for translational dynamics

The output feedback control for translational dynamics is designed based on the estimates from the EHGO. To overcome the mechanical underactuation, ϕ_1 and θ_1 are taken as virtual inputs $\phi_v = \phi_1$ and $\theta_v = \theta_1$ provided by the rotational dynamics, which is in a faster time scale than translational dynamics. The control inputs for the translational dynamics are ϕ_v, θ_v, and u_1. The control inputs are [26,27]

$$\begin{aligned} u_1 &= -\frac{m(f_z - g)}{\cos\phi_v \cos\theta_v}, \\ \phi_v &= \tan^{-1}\left(\frac{(f_x \sin\psi_r - f_y \cos\psi_r)\cos\theta_v}{f_z - g}\right), \\ \theta_v &= \tan^{-1}\left(\frac{f_y \sin\psi_r + f_x \cos\psi_r}{f_z - g}\right) \end{aligned} \tag{12}$$

where

$$\begin{bmatrix} f_x \\ f_y \\ f_z \end{bmatrix} = \begin{bmatrix} -k_{x_1}(x_1 - x_r) - k_{x_2}(\hat{x}_{2s} - \dot{x}_r) + \ddot{x}_r - \hat{\sigma}_{xs} \\ -k_{y_1}(y_1 - y_r) - k_{y_2}(\hat{y}_{2s} - \dot{y}_r) + \ddot{y}_r - \hat{\sigma}_{ys} \\ -k_{z_1}(z_1 - z_r) - k_{z_2}(\hat{z}_{2s} - \dot{z}_r) + \ddot{z}_r - \hat{\sigma}_{zs} \end{bmatrix},$$

k_{i_1} and k_{i_2} are chosen such that the polynomials, $s^2 + k_{i_2} s + k_{i_1}$ for $i = x, y, z$, are Hurwitz. Here, $\hat{\imath}_{2s}$ and $\hat{\sigma}_{is}$ for $i = x, y, z$ are the same as (11).

4. Stability analysis of the closed-loop system

In this section, we will show the stability analysis of the closed-loop system based on the Lyapunov analysis. First, we will define the error variables of the closed-loop system, which consists of translational dynamics, rotational dynamics, output feedback controllers, and EHGO. Second, the closed-loop system is derived as the singularly perturbed form for the stability analysis.

4.1. Error dynamics of extended high-gain observer

The error variables of the EHGO are $\eta = [\eta_X^T, \eta_\Theta^T]^T$, where

$$\eta_i = [\eta_{i_1}, \eta_{i_2}, \eta_{i_3}]^T, \ \eta_{i_1} = \frac{i_1 - \hat{\imath}_1}{\varepsilon_3^2}, \ \eta_{i_2} = \frac{i_2 - \hat{\imath}_2}{\varepsilon_3}, \ \eta_{i_3} = \sigma_i(t) - \hat{\sigma}_i(t)$$

for $i = x, y, z, \phi, \theta, \psi$. The EHGO error dynamics is written as

$$\varepsilon_3 \dot{\eta} = A_\eta \eta + \varepsilon_3 \left[\bar{B}_1 \Delta_1 + \bar{B}_2 \Delta_2\right], \tag{13}$$

where the matrices $A_\eta = \text{block diag}[\Lambda_x, \Lambda_y, \Lambda_z, \Lambda_\phi, \Lambda_\theta, \Lambda_\psi] \in \mathbb{R}^{18\times 18}$, $\bar{B}_1 = \text{block diag}\ [B_{e_1}, \ldots, B_{e_1}] \in \mathbb{R}^{18\times 6}$, and $\bar{B}_2 = \text{block diag}\ [B_{e_2}, \ldots, B_{e_2}] \in \mathbb{R}^{18\times 6}$ are given by

$$\Lambda_i = \begin{bmatrix} -\alpha_{i1} & 1 & 0 \\ -\alpha_{i2} & 0 & 1 \\ -\alpha_{i3} & 0 & 0 \end{bmatrix}, \ B_{e_1} = [0,1,0]^T, \ B_{e_2} = [0,0,1]^T,$$

and Δ_i for $i = 1, 2, 3$ are

$$\Delta_1 = \begin{bmatrix} (F_X(\Theta, u_1) - F_X(\hat{\Theta}, u_1))/\varepsilon_3 \\ (F_\Theta(\Theta, U_R) - F_\Theta(\hat{\Theta}, U_R))/\varepsilon_3 \end{bmatrix}, \quad \Delta_2 = \begin{bmatrix} \dot{\sigma}_X \\ \dot{\sigma}_\Theta \end{bmatrix}.$$

We note that the disturbances, σ_i for $i = x, y, z, \phi, \theta, \psi$, need to be continuously differentiable as described in Assumption 1. The components of Δ_1, i.e., $F_X(\Theta, u_1) - F_X(\hat{\Theta}, u_1)$ and $F_\Theta(\Theta, U_R) - F_\Theta(\hat{\Theta}, U_R)$, have the bounds $\|F_X(\Theta, u_1) - F_X(\hat{\Theta}, u_1)\| \leq \varepsilon_3 \|\eta\|$ and $\|F_\Theta(\Theta, U_R) - F_\Theta(\hat{\Theta}, U_R)\| \leq \varepsilon_3 \|\eta\|$. Δ_2 have the bounds $\|\Delta_2\| \leq k_{\delta_1}$ with $k_{\delta_1} > 0$.

4.2. Error dynamics of rotational controller (RLS-DI)

The error variable for the RLS-DI is $s_r = U_R - U_R^*$ where U_R^* is the solution of (5). The error dynamics of the RLS-DI are written as

$$\varepsilon_2 \dot{s}_r = -P^T \mathbf{F}_\Theta(t, \Theta, U_R^* + s_r) + \Delta_{\sigma_\Theta} + \Delta_\Theta - \varepsilon_2 \dot{U}_R^*, \tag{14}$$

where

$$\Delta_{\sigma_\Theta} = \begin{bmatrix} \hat{\sigma}_{\phi s} - \sigma_\phi \\ \hat{\sigma}_{\theta s} - \sigma_\theta \\ \hat{\sigma}_{\psi s} - \sigma_\psi \end{bmatrix}, \ \Delta_\Theta = \begin{bmatrix} k_{\phi_2}(\hat{\phi}_{2s} - \phi_2) \\ k_{\theta_2}(\hat{\theta}_{2s} - \theta_2) \\ k_{\psi_2}(\hat{\psi}_{2s} - \psi_2) \end{bmatrix}$$

4.3. Error dynamics of rotational dynamics

The rotational error variable is $e_\Theta = [e_\phi^T, e_\theta^T, e_\psi^T]^T$ where

$$e_i = [e_{i_1}, e_{i_2}]^T, \quad e_{i_1} = i_1 - i_r, \quad e_{i_2} = \varepsilon_1(i_2 - i_{r_2}),$$

for $i = \phi, \theta, \psi$. The rotational error dynamics is formulated as

$$\varepsilon_1 \dot{e}_\Theta = A_\Theta e_\Theta + B[k_1(\Theta_v - \Theta_r) + \varepsilon_1^2 \mathbf{F}_\Theta - \varepsilon_1^2 \ddot{\Theta}_r - \varepsilon_1 k_2 \dot{\Theta}_r], \tag{15}$$

where $\Theta_v = [\phi_v, \theta_v, \psi_r]^T$, and $A_\Theta = (A - BL_\Theta)$ with $L_\Theta = \text{block diag}\ [L_\phi, L_\theta, L_\psi]$ with $L_i = [k_{i_1}, k_{i_2}]$ for $i = \phi, \theta, \psi$.

4.4. Error dynamics of translational dynamics

We begin by defining the translational error variable $e_X = X - X_r$ where $X_r = [x_r, \dot{x}_r, y_r, \dot{y}_r, z_r, \dot{z}_r]^T$. The translational error dynamics are written as

$$\begin{aligned} \dot{e}_X &= A_X e_X + B[F_{X_1} + F_{X_2}], \\ F_{X_1} &= f_X(\Theta, u_1) - f_X(\Theta_v, u_1), \\ F_{X_2} &= f_X(\Theta_v, u_1) - f_X(\Theta_r, u_1), \end{aligned} \tag{16}$$

where $A_X = A - BL_X$, L_X = block diag$[L_x, L_y, L_z]$ and $L_i = [k_{i_1}, k_{i_2}]$ for $i = x, y, z$.

Now, we will analyze the multi-time-scale structure of the closed-loop systems (13)–(16). The steady state of each subsystem is investigated by sequentially introducing the boundary layer system from the fastest to the slowest subsystems. Let (13) be the fastest subsystem and other subsystems as the slow. The boundary layer system of (13) is obtained by setting $\varepsilon_3 = 0$ on the right-hand side of (13) as

$$\varepsilon_3 \dot{\eta} = A_\eta \eta,$$

which is exponentially stable at $\eta = 0$. With the quasi-steady state η, let (14) be the fastest subsystem among the subsystems of the reduced system consisting of (14)–(16). We have the boundary layer system of (14) by setting $\varepsilon_2 = 0$ on the right-hand side of (14) and letting $\eta = 0$, $\varepsilon_3 = 0$ as

$$\varepsilon_2 \dot{s}_r = -P^T \mathbf{F}_\Theta(t, \Theta, U_R^* + s_r).$$

To analyze the stability, we define a Lyapunov function of the rotational controller as $V_d = s_r^T P s_r$. By taking the derivative of the Lyapunov function with respect to time and using (6) such that K is P, we have

$$\dot{V}_d = -\left(\frac{2}{\varepsilon_2}\right) s_r^T P^T \mathbf{F}_\Theta - s_r^T P^T P s_r \le -\left(\frac{2}{\varepsilon_2}\right) s_r^T s_r - s_r^T P^T P s_r,$$

which is asymptotically stable at $s_r = 0$. With the quasi-steady state η and s_r, consider that subsystem (15) is the fastest subsystem among the reduced system consisting of (15) and (16). The boundary layer system of (15) is obtained by setting $\varepsilon_1 = 0$ on the right-hand side of (15) as

$$\varepsilon_1 \dot{e}_\Theta = A_\Theta e_\Theta,$$

which is exponentially stable at $e_\Theta = 0$. The boundary layer system of the remaining subsystem (16) is

$$\dot{e}_X = A_X e_X,$$

which is exponentially stable at $e_X = 0$.

Theorem 1. *For closed-loop systems (13)–(16), suppose that Assumptions 1 and 2 are satisfied. Choose compact sets $\mathbf{X}_1 \subset \mathbb{R}^{12}$ in the domain $D_X \times D_\Theta$, $\mathbf{X}_2 \subset \mathbb{R}^3$, $\mathbf{X}_3 \subset \mathbb{R}^{12}$, and $\mathbf{X}_4 \subset \mathbb{R}^6$. Suppose that all trajectories $(X, \Theta, U_R, \hat{X}, \hat{\Theta}, \hat{\sigma}_X, \hat{\sigma}_\Theta)$ start from $(X(0), \Theta(0)) \in \mathbf{X}_1$, $U_\Theta(0) \in \mathbf{X}_2$, $(\hat{X}(0), \hat{\Theta}(0)) \in \mathbf{X}_3$, and $(\hat{\sigma}_X(0), \hat{\sigma}_\Theta(0)) \in \mathbf{X}_4$. Then, there exists $\varepsilon^* > 0$ such that for*

$$\varepsilon_1 < \varepsilon^*, \quad \varepsilon_2 < \varepsilon^*, \quad \varepsilon_3 < \varepsilon^*, \quad \frac{\varepsilon_2}{\varepsilon_1} < \varepsilon^*, \quad \frac{\varepsilon_3}{\varepsilon_2} < \varepsilon^*, \tag{17}$$

- *all trajectories are bounded;*
- *$\|X - X_r\| \to 0$ and $\|U_R - U_R^*\| \to 0$ as ε_1 in (10) and (15), ε_2 in (7) and (14), ε_3 in (4) and (13), $(\varepsilon_2/\varepsilon_1)$, and $(\varepsilon_3/\varepsilon_2)$ approach zero for all $t \ge 0$.*

Proof. We define Lyapunov functions of each multi-time-scale system for the stability analysis of the closed-loop system.

$$V_X = e_X^T P_X e_X, \; V_\Theta = e_\Theta^T P_\Theta e_\Theta, \; V_r = \mathbf{F}_\Theta^T \mathbf{F}_\Theta, \; V_\eta = \eta^T P_\eta \eta, \tag{18}$$

where P_i are found by solving $A_i^T P_i + P_i A_i = -Q_i$ with $i = X, \Theta, \eta$, and A_X, A_Θ, and A_η are defined in (13), (15), and (16), respectively.

We define the following domains in which we will conduct the stability analysis of the closed-loop system

$$\begin{aligned} \Omega_a &= \{V_X \le a_1\} \times \{V_\Theta \le a_2\} \times \{V_r \le a_3\}, \\ \Omega_b &= \{V_X \le b_1\} \times \{V_\Theta \le b_2\} \times \{V_r \le b_3\}, \\ \Omega_c &= \{V_X \le c_1\} \times \{V_\Theta \le c_2\}, \end{aligned} \tag{19}$$

where $0 < a_1 < b_1 < c_1$, $0 < a_2 < b_2 < c_2$, and $0 < a_3 < b_3$. We use a multi-time-scale separation approach in which the dynamics are split into the subsystems described earlier, and we utilize the sets in (19) for this analysis.

First, we show that all trajectories enter a positively invariant set using the Lyapunov functions in (18) for each subsystem. A brief description of the proof for this work is similar to that shown in earlier work on high-gain observers and DI, e.g., [22] as follows

- Initially, the trajectories (e_X, e_Θ, s_r) and η starting from $(e_X(0), e_\Theta(0), s_r(0)) \in \Omega_a$ and $\eta(0)$ which lies outside of the set $\{V_\eta \in \rho\varepsilon_3^2\}$, enter the set $\Omega_b \times \{V_\eta \le \rho_1 \varepsilon_3^2\}$.
- Next, the trajectories (e_X, e_Θ, s_r) and η starting from within $\Omega_b \times \{V_\eta \le \rho\varepsilon_3^2\}$ enter the set $\Omega_c \times \{V_r \le \rho_2\mu_1^2\} \times \{V_\eta \le \rho_1\varepsilon_3^2\}$ with $\mu_1 = (\varepsilon_2/\varepsilon_1)$.
- Finally, the trajectories (e_X, e_Θ, s_r) and η starting from within $\Omega_c \times \{V_r \le \rho_2\mu_1^2\} \times \{V_\eta \le \rho_1\varepsilon_3^2\}$ enter the set $\{V_X \le e_1\} \times \{V_\Theta \le e_2\varepsilon_1^2\} \times \{V_r \le \rho_2\mu_1^2\} \times \{V_\eta \le \rho_1\varepsilon_3^2\}$, where e_1 and e_2 are positive constants.

Since all three steps above are similar, we will only prove the first bullet. In the first bullet, the initial trajectories (e_X, e_Θ, s_r) and η start from the set $(e_X(0), e_\Theta(0), s_r(0)) \in \Omega_a$ and $\eta \notin \{V_\eta \in \rho\varepsilon_3^2\}$ where $\|\eta(0)\| \le (k/\varepsilon_3^2)$. The derivative of V_η with respect to time along the trajectories (13)–(16) is as follows.

$$\dot{V}_\eta = -\left(\frac{1}{\varepsilon_3}\right) \eta^T \eta + \left(\bar{B}_1 \Delta_1 + \bar{B}_2 \Delta_2\right)^T P_\eta \eta.$$

Using the boundness of the term $(\bar{B}_1\Delta_1 + \bar{B}_2\Delta_2)$ in (13) for all $(e_X, e_\Theta, s_r) \in \Omega_a$, we obtain

$$\begin{aligned} \dot{V}_\eta &\le -\frac{1}{\varepsilon_3}\|\eta\|^2 + k_{o_1}\|\eta\|^2 + k_{o_2}\|\eta\| \\ &\le -\frac{1}{2\varepsilon_3}\|\eta\|^2 + k_{o_2}\|\eta\| \quad \text{for} \quad \varepsilon_3 < \frac{1}{2k_{o_1}} \end{aligned} \tag{20}$$

where k_{o_i} for $i = 1, 2$ are positive constants. With $\varepsilon_3 < 1/(2k_{o_1})$,

$$\dot{V}_\eta \le -\left(\frac{\gamma_1}{\varepsilon_3}\right) V_\eta, \quad \text{for} \quad V_\eta \ge \rho_1 \varepsilon_3^2$$

where $\rho_1 = P_{\eta_m}\gamma_2^2$ for some $\gamma_1 > 0$ and $\gamma_2 > 0$, and $P_{\eta_m} = \lambda_{max}(P_\eta)$. For the second bullet, since the trajectory η is restricted to the set $\{V_\eta \le \rho_1\varepsilon_3^2\}$, η has the upper bound, $\|\eta\| \le 4k_{o_3}\varepsilon_3$ for positive constant k_{o_3}. With this upper bound, a similar procedure can be used to prove the second and third bullet, so those proofs are omitted.

Next, we will prove that the size of the ultimate boundedness can be arbitrarily small with sufficient small control parameters, $0 < \varepsilon_3 \ll \varepsilon_2 \ll \varepsilon_1 < 1$. The derivative of the Lyapunov function V_X and V_Θ along the trajectories (13)–(16) are as follows.

$$\begin{aligned} \dot{V}_X &= -e_X^T e_X + 2\left[F_{X_1} + F_{X_2}\right]^T B^T P_X e_X \\ &\le -\|e_X\|^2 + 2P_{X_m}\left(k_{X_1}\|e_\Theta\| + k_{X_2}\right)\|e_X\|, \end{aligned} \tag{21}$$

$$\begin{aligned} \dot{V}_\Theta &= -\left(\frac{1}{\varepsilon_1}\right) e_\Theta^T e_\Theta \\ &\quad + 2\left[\varepsilon_1\left(\mathbf{F}_\Theta^T - \dot{\Theta}_r^T\right) - k_2\dot{\Theta}_r^T + \left(\frac{2k_1}{\varepsilon_1}\right)\left(\Theta_v - \Theta_r\right)^T\right] B^T P_\Theta e_\Theta \\ &\le -\left(\frac{1}{\varepsilon_1}\right)\|e_\Theta\|^2 + \left[\varepsilon_1 k_{\Theta_1}\left(\|\mathbf{F}_\Theta\| + \Theta_{r_1}\right) + k_{\Theta_2}\Theta_{r_2}\right]\|e_\Theta\| \end{aligned} \tag{22}$$

where $\|P_X\| \le P_{X_m}$, Θ_{r_1} and Θ_{r_2} are the rotational reference and its derivatives, respectively. k_{X_i} for $i = 1, 2$ and k_{Θ_i} for $i = 1, 2$ are some positive constant.

The derivative of V_r with respect to time is

$$\begin{aligned}\dot{V}_r =& -\left(\frac{1}{\varepsilon_2}\right)\mathbf{F}_\Theta^T\left(\frac{\partial \mathbf{F}_\Theta}{\partial U_R}\right)\left(\frac{\partial \mathbf{F}_\Theta}{\partial U_R}\right)^T\mathbf{F}_\Theta \\ &-\left(\frac{1}{\varepsilon_2}\right)\mathbf{F}_\Theta^T\left(\frac{\partial \mathbf{F}_\Theta}{\partial U_R}\right)\left(\frac{\partial \mathbf{F}_\Theta}{\partial U_R}\right)^T\left[\mathbf{F}_{\Theta_s}-\mathbf{F}_\Theta\right] \\ &+\mathbf{F}_\Theta^T\left[\left(\frac{\partial \mathbf{F}_\Theta}{\partial \psi_r}\right)\dot{\psi}_r+\left(\frac{\partial \mathbf{F}_\Theta}{\partial \sigma_\Theta}\right)\dot{\sigma}_\Theta\right] \\ &+\mathbf{F}_\Theta^T\left(\frac{\partial \mathbf{F}_\Theta}{\partial \Theta}\right)\left\{\left(\frac{1}{\varepsilon_1}\right)\left[A_\Theta e_\Theta+k_1 B\left(\Theta_d-\Theta_r\right)\right]\right. \\ &\qquad\left.+\left[\varepsilon_1\left(\mathbf{F}_\Theta-\ddot{\Theta}_r\right)+\dot{\Theta}_r+\tilde{\Theta}_r\right]\right\} \\ \le& -\left(\frac{k_{r_1}}{\varepsilon_2}\right)\|\mathbf{F}_\Theta\|^2+\left(\frac{k_{r_2}}{\varepsilon_2}\right)\|\mathbf{F}_\Theta\|\left(\Delta_{\sigma_\Theta}+\Delta_\Theta\right) \\ &+\left[\left(\frac{1}{\varepsilon_1}\right)k_{r_3}\|e_\Theta\|+\varepsilon_1 k_{r_4}\left(\|\mathbf{F}_\Theta\|+k_{r_5}\Theta_r\right)\right]\|\mathbf{F}_\Theta\|+\bar{\Theta}_2\|\mathbf{F}_\Theta\|\end{aligned} \tag{23}$$

where k_{r_i} for $i=1,\ldots,5$ are positive constants. Note that Δ_{σ_Θ} and Δ_Θ are bounded as $\Delta_{\sigma_\Theta}\le k_{\Theta_6}\|\eta\|$ and $\Delta_{\sigma_\Theta}\le\varepsilon_3 k_{\Theta_7}\|\eta\|$, respectively, after the system passes the transient period of the EHGO.

Now we will show the stability of the entire coupled subsystem using the method in Section 9.3 of [28] with (20)–(23). We define $S_1=\sqrt{V_X}$, $S_2=\sqrt{V_\Theta}$, $S_3=\sqrt{V_r}$, $S_4=\sqrt{V_\eta}$ and take the upper right-hand derivative $D^+(\cdot)$ of each variable, resulting in

$$\begin{aligned}D^+S_1 &\le -k_{a_1}S_1+k_{a_2}S_2+k_{a_3}S_3 \\ D^+S_2 &\le -\left(\frac{k_{b_1}}{\varepsilon_1}\right)S_2+\varepsilon_1 k_{b_2}S_3+\varepsilon_1 k_{b_4}\delta_1(t)+k_{b_5}\delta_2(t) \\ D^+S_3 &\le -\left(\frac{k_{c_1}}{\varepsilon_2}-\varepsilon_1 k_{c_2}\right)S_3+\left(\frac{k_{c_3}+k_{c_4}\varepsilon_3}{\varepsilon_2}\right)S_4 \\ &\quad+\left(\frac{k_{c_5}}{\varepsilon_1}\right)S_1+\varepsilon_1 k_{c_6}\delta_3(t)+k_{c_7}\delta_4(t) \\ D^+S_4 &\le -\left(\frac{k_{d_1}}{\varepsilon_3}\right)S_4+k_{d_3}\delta_5(t)\end{aligned} \tag{24}$$

where the positive constants δ_i for $i=1,\ldots,5$ are nonvanishing perturbations, and the positive constants k_{p_i} for $p=a,b,c,d$ and $i=1,\ldots,7$ are independent on ε_1, ε_2, and ε_3. (24) can be formed as a matrix form as

$$D^+S\le -HS+\varepsilon_1 Z_1+Z_2$$

where

$$\begin{aligned}D^+S &= \left[D^+S_1, D^+S_2, D^+S_3, D^+S_4\right]^T, \\ S &= [S_1,S_2,S_3,S_4]^T, \\ Z_1 &= \left[0,\ k_{b_4}\delta_1(t),\ k_{c_6}\delta_3(t),\ 0\right]^T, \\ Z_2 &= \left[0,\ k_{b_5}\delta_2(t), k_{c_7}\delta_4(t), k_{d_5}\delta_5(t)\right]^T.\end{aligned}$$

H is quasi-monotone increasing [29] with $0<\varepsilon_3\ll\varepsilon_2\ll\varepsilon_1<1$ because the off-diagonal components of H are positive, as explained similarly in Appendix B of [22]. Now consider the differential equation with respect to the control inputs $U=\left[u_1,u_2,u_3,u_4\right]^T$ as

$$\dot{U}=-HU+\varepsilon_1 Z_1+Z_2 \tag{25}$$

with initial conditions $U(0)=S(0)$. We can show that $S\le U$ for $\forall t>0$ and that the steady state of (25) is $H^{-1}\left(\varepsilon_1 Z_1+Z_2\right)$ using the vectorial comparison method presented in Chapter IX of [29]. Thus, we can conclude that the size of the ultimate boundedness can be made arbitrarily small since the ultimate boundedness is dependent on ε_i for $i=1,2,3$. □

5. Numerical simulation results

The proposed output feedback controller is validated through numerical simulation. The objective of the simulation is to evaluate the tracking performance of the proposed controller along the reference trajectories, $f_r=[5\sin t,\ 5\cos t,\ 5\sin t]^T$, and $\psi_d=0$ in the presence of the external disturbances $\sigma_X=[-3\sin 2t,\ -3\sin 2t,\ -3\sin 2t]^T$ and $\sigma_\Theta=[\cos t,\ \cos t,\ \cos t]^T$. The system parameters were $m=1$ kg, $I_{xx}=0.0093$ kg m^2, $I_{yy}=0.0107$ kg m^2, and $I_{zz}=0.0195$ kg m^2. The control gains for the plant and reference systems are $k_{x_1}=k_{y_1}=k_{z_1}=7, k_{x_2}=k_{y_2}=k_{z_2}=3$, $k_1=50$, and $k_2=10$. The control parameters are $\varepsilon_1=0.18$, $\varepsilon_2=0.001$, and $\varepsilon_3=0.0001$ which are chosen to satisfy (17). The observer gains are $\alpha_{i1}=\alpha_{i2}=3$, $\alpha_{i3}=1$, $\alpha_{j1}=\alpha_{j2}=5$, and $\alpha_{j3}=1$, for $i=x,y,z$, and $j=\phi,\theta,\psi$. The initial conditions for the system states in the numerical simulation are

$$\begin{aligned}&x_1(0)=1,\ \ x_2(0)=0.2,\ \ y_1(0)=1,\ \ y_2(0)=-0.1,\\ &z_1(0)=1,\ \ z_2(0)=0.1,\ \ \phi_1(0)=0,\ \ \phi_2(0)=0,\\ &\theta_1(0)=0,\ \ \theta_2(0)=0,\ \ \psi_1(0)=0,\ \ \psi_2(0)=0,\end{aligned}$$

The initial conditions of the RLS-DI are

$$u_2(0)=48,\ u_3(0)=0.5,\ u_4(0)=0.5,\ P_0=I_3.$$

The initial conditions of the EHGO are

$$\begin{aligned}&\hat{x}_1(0)=\hat{x}_2(0)=\hat{y}_1(0)=\hat{y}_2(0)=\hat{z}_1(0)=\hat{z}_2(0)=0,\\ &\hat{\sigma}_x(0)=\hat{\sigma}_y(0)=\hat{\sigma}_z(0)=0,\ \ \hat{\phi}_1(0)=\hat{\theta}_1(0)=\hat{\psi}_1(0)=1,\\ &\hat{\phi}_2(0)=0.1,\ \ \hat{\psi}_2(0)=0,\ \ \hat{\theta}_2(0)=1,\\ &\hat{\sigma}_\theta(0)=1,\ \ \hat{\sigma}_\phi(0)=0.1,\ \ \hat{\sigma}_\psi(0)=0.\end{aligned}$$

In Fig. 3(a), the translational trajectories x_1, y_1, and z_1 and the translational references x_r, y_r, and z_r are shown. Excellent tracking is achieved even in the presence of unknown external disturbances σ_X and σ_Θ. In Fig. 3(b), trajectories ϕ_v, and θ_v from the RLS-DI and the reference ψ_d are indistinguishable from the trajectories ϕ_1, θ_1, and ψ_1. The four control inputs u_1, u_2, u_3, and u_4 are shown in Fig. 3(c). In Figs. 3(g) and 3(h), Θ and $\hat{\Theta}$ are indistinguishable. The results shown in Fig. 3(i) indicate that the EHGO successfully estimates the rotational disturbances, σ_Θ. In Figs. 3(d) and 3(e), $\hat{X}$ is on top of the estimates X. The results shown in Fig. 3(f) present that the EHGO successfully estimates the translational disturbances σ_X. At the beginning of the simulation in Figs. 3(e)–3(i), the peaking phenomena are shown and quickly disappear due to the high gains of the EHGO.

In Fig. 4, the EHGO-FL [24], DOB-CSMC, and EHGO-RLS-DI are compared by perturbing the input Jacobian. The same diagonal matrix is added on each of the input Jacobian for perturbation. While the EHGO-RLS-DI and the EHGO-FL successfully track the references, the DOB-CSMC is degraded. To show the effectiveness of the EHGO-RLS-DI over the EHGO-FL, we utilized the sum of the root-mean-square error (RMSe) over the experiment time duration as a performance parameter, i.e., RMSe = rms(x_1-x_r) + rms(y_1-y_r) + rms(z_1-z_r) + rms$(\psi_r-\psi_1)$. The results shown in Table 1 indicate that the proposed EHGO-RLS-DI outweighs the EHGO-FL by 15.78%. The outperformance of the EHGO-RLS-DI is because the RLS method recursively computes the input Jacobian's coefficient P according to (7) in the direction of attenuating the perturbations.

Table 1
RMSe values of the DOB-CSMC, EHGO-FL, and EHGO-RLS-DI.

	DOB-CSMC	EHGO-FL	EHGO-RLS-DI
RMSe	Degrated	3.7084	3.1233

6. Hardware implementation

6.1. Control design in discrete time

For the hardware implementation, we discretized the proposed controller using the forward difference method with sampling time

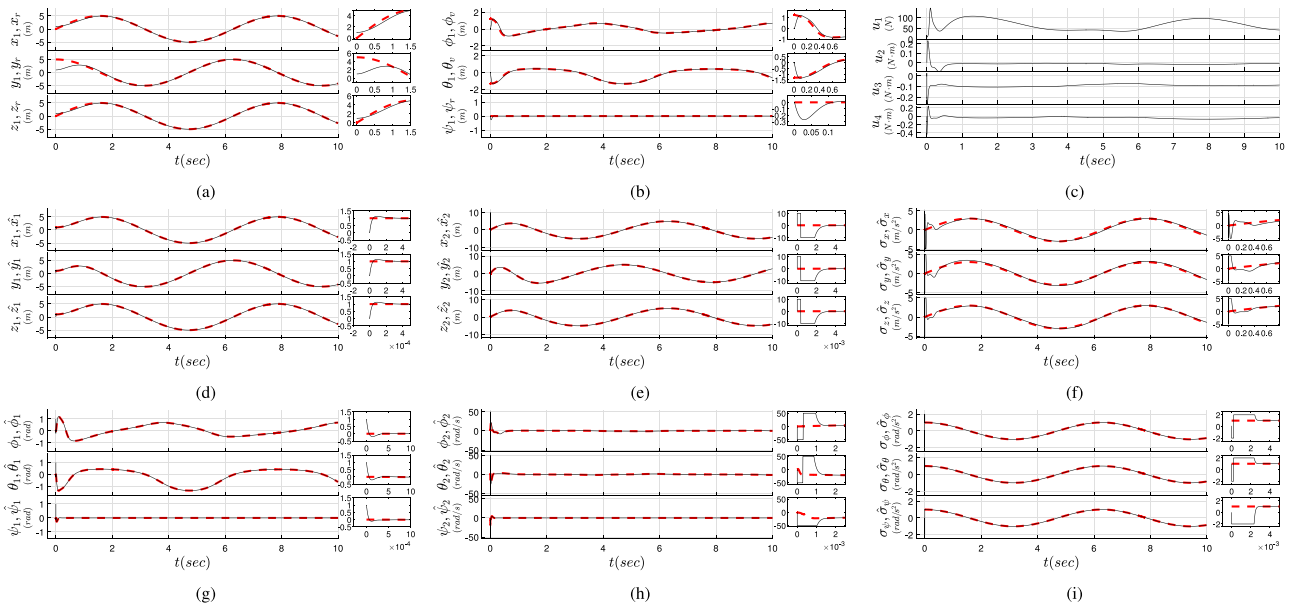

Fig. 3. Note that the red dashed lines are references and the solid black lines are the estimates or states. **(a)** The references x_r, y_r, and z_r and states x_1, y_1, and z_1 are plotted. **(b)** The references ϕ_v, θ_v, and ψ_r and states ϕ_1, θ_1, and ψ_1 are plotted. **(c)** The control inputs u_1, u_2, u_3, u_4 are plotted. **(d)** The states x_1, y_1, and z_1 and estimates $\hat{x}_1$, $\hat{y}_1$, and $\hat{z}_1$ are plotted. **(e)** The states x_2, y_2, and z_2 and estimates $\hat{x}_2$, $\hat{y}_2$, and $\hat{z}_2$ are plotted. **(f)** The disturbances σ_x, σ_y, and σ_z and estimates $\hat{\sigma}_x$, $\hat{\sigma}_y$, and $\hat{\sigma}_z$ are plotted. **(g)** The states ϕ_1, θ_1, and ψ_1 and estimates $\hat{\phi}_1$, $\hat{\theta}_1$, and $\hat{\psi}_1$ are plotted. **(h)** The states ϕ_2, θ_2, and ψ_2 and estimates $\hat{\phi}_2$, $\hat{\theta}_2$, and $\hat{\psi}_2$ are plotted. **(i)** The disturbances σ_ϕ, σ_θ, and σ_ψ and estimates $\hat{\sigma}_\phi$, $\hat{\sigma}_\theta$, and $\hat{\sigma}_\psi$ are plotted. The initial part of the time was enlarged and plotted to the right of each plot.

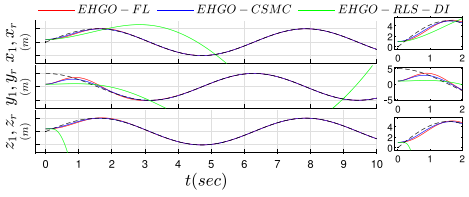

Fig. 4. Given the references, the performance of the EHGO-FL (solid red line), the DOB-CSMC (solid green lines), and the EHGO-RLS-DI (solid blue lines) with a perturbation are compared.

$T = 0.004$ (s). The EHGO in (3) is discretized as follows

$$\begin{aligned}
\hat{X}_{k+1} &= \hat{X}_k + T[A\hat{X}_k + B\left(F_X(\hat{X}, u_1) + \hat{\sigma_X}(t)\right) + H_x(\varepsilon_3)(y_x - C\hat{X})],\\
\hat{\sigma}_{X_{k+1}} &= \hat{\sigma}_{X_k} + T[H_{x_e}(y_x - C\hat{X})],\\
\hat{\Theta}_{k+1} &= \hat{\Theta}_k + T[A\hat{\Theta}_k + B\left(F_\Theta(\hat{\Theta}, U_R) + \hat{\sigma}_\Theta(t)\right) + H_\theta(\varepsilon_3)(y_\theta - C\hat{\Theta})],\\
\hat{\sigma}_{\Theta_{k+1}} &= \hat{\sigma}_{\Theta_k} + T[H_{\theta_e}(y_\theta - C\hat{\Theta})],
\end{aligned} \tag{26}$$

where T is the sampling period, and estimates of X and Θ are $\hat{X}_k = [\hat{X}_x^T, \hat{X}_y^T, \hat{X}_z^T]^T$ and $\hat{\Theta}_k = [\hat{\Theta}_\phi^T, \hat{\Theta}_\theta^T, \hat{\Theta}_\psi^T]^T$, respectively. The high gains of the EHGO are the same as the continuous time system in (4). The output feedback controller for the translational dynamics is the same as in (12) utilizing the estimates of the states and disturbances from the EHGO.

The output feedback controller for the rotational dynamics is

$$\begin{aligned}
U_{R_{k+1}} &= U_{R_k} - \left(\frac{T}{\varepsilon_2}\right) P^T \mathbf{F}_{\hat{\Theta}_s}, \quad U_{R_0} = U_R(0),\\
P_{k+1} &= P_k - \left(\frac{T}{\varepsilon_2}\right) P^T P, \quad P_0 = P(0).
\end{aligned} \tag{27}$$

In the real system, the control inputs consist of the thrust force u_1 and torques u_2, u_3, and u_4 are mapped into four thrust forces corresponding to four propellers of the quadrotor. This mapping will be explained in detail in Section 6.3.

As a demonstration of the time responses of the discrete time control system, we discretized the proposed controller as shown in (26) and (27) and conducted the discrete time numerical simulation. The sampling rate is 250 Hz, the same as the sensor sampling rate of the hardware configuration that will be elaborated in Section 6.2. The control gains for the plant and reference system are $k_{x_1} = k_{y_1} = k_{z_1} = 22$, $k_{x_2} = k_{y_2} = k_{z_2} = 6$, $k_1 = 50$, and $k_2 = 10$. The control parameters are $\varepsilon_1 = 0.21$, $\varepsilon_2 = 0.03$, $\varepsilon_3 = 0.025$, which satisfy (17). The initial condition of P_0 in (7) is chosen as $P_0 = I_3$ where $I_3 \subset \mathbb{R}^{3\times3}$ is an identity matrix. The EHGO gains defined in (4) are $\alpha_{i1} = \alpha_{i2} = 5$, $\alpha_{i3} = 1$, $\alpha_{j1} = \alpha_{j2} = 3$, $\alpha_{j3} = 1$. With these values, the rise time, peak time, and settling time are 0.628, 0.848, and 1.5 s, respectively.

6.2. Hardware configuration

We used a Pixhawk-4 Flight Management Unit (FMU) to implement the proposed controller. The FMU contains accelerometers, gyroscopes, a magnetometer, a barometer, and a GPS. All sensors except GPS are encapsulated within the Pixhawk FMU, while the GPS is connected externally. An Extended Kalman Filter fuses the sensor data and provides necessary signals, such as x_1, y_1, z_1, x_2, y_2, z_2, ϕ_1, θ_1, ψ_1, ϕ_2, θ_2, and ψ_2. The signal z_1 is mainly provided by the barometer. All sensors are operated at a fixed sampling rate of 250 Hz. To minimize the disturbance from vibrations, the FMU is placed on a vibration-damping board. For actuators, we used four 810 kV motors with four 40 A Electronic Speed Controllers (ESCs) and four 10×4.5 carbon fiber rotors. A three-cell 2200 mAh Lithium Polymer battery is used as a power source. A detailed configuration of the quadrotor is shown in Fig. 5.

6.3. Actuator mapping and system parameter measurement

Since the control signals indicate the torque along the three body axes and vertical thrust force, the control signals need to be converted into rotor force signals. Requested forces f_i for $i = 1, \ldots, 4$ corresponding to four actuators are mapped to control signals as follows.

$$f_i(k+1) = \frac{u_1(k+1)}{4} - \frac{u_2(k+1)}{4d} + \frac{u_3(k+1)}{4d} + \frac{u_4(k+1)}{4c} \tag{28}$$

where $i = 1, \ldots, 4$ are the index of each motor, and $d = 0.153$ (m) is the distance between the actuator and the center of mass of the airframe

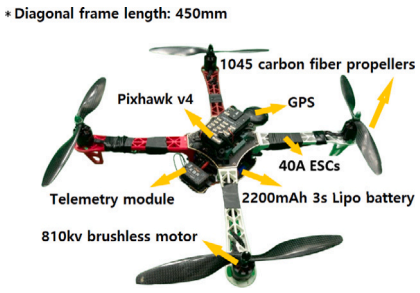

Fig. 5. Sensor connection configuration of the quadrotor.

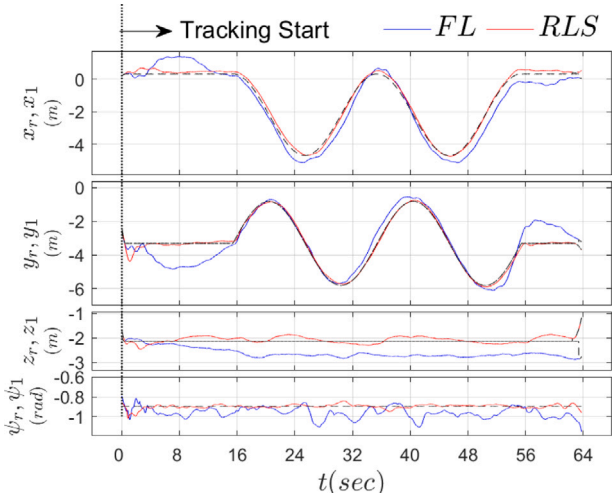

Fig. 6. Trajectories x_1, y_1, and z_1 of EHGO-RLS (red solid lines) and EHGO-FL (blue solid lines), and references x_r, y_r, z_r (black dashed lines) of the outdoor experiment are plotted.

Fig. 7. The frame-by-frame time lapses images of the hardware experiment.

in the x and y directions. c is the drag coefficient of the rotors, found to be 0.1. Note that the thrust force u_1 is equally distributed into four motors, and the rolling and pitching torques corresponding to u_2 and u_3 are converted into forces by dividing with moment arm d. The yawing torque u_4 is scaled by the drag coefficient c. Then, the desired forces are mapped to PWM signals, and the function between forces and PWM signals is obtained experimentally. We use a load cell with Arduino to measure the thrust force of the motor. The function is obtained as follows.

$$M_i(k) = G_1 f_i^3(k) + G_2 f_i^2(k) + G_3 f_i(k) + G_4$$

for $i = 1, \ldots, 4$, where $G_1 = 2.269 \times 10^{-7}$, $G_2 = -3.5 \times 10^{-3}$, $G_3 = 2.598 \times 10^{-3}$, and $G_4 = 9.676 \times 10^3$. The moment of inertia is found to be $I_{xx} = 0.0134$ kg/m^2, $I_{yy} = 0.0143$ kg/m^2, and $I_{zz} = 0.0235$ kg/m^2 obtained by trifilar pendulum experiment as described in [30]. The mass of the quadrotor $m = 1.164$ kg.

Table 2
RMSe values of EHGO-FL and EHGO-RLS-DI for hardware experiments.

	EHGO-RLS-DI	EHGO-FL
x_1	0.1664	0.2999
y_1	0.1497	0.2130
z_1	0.1399	0.2198
ψ	0.0215	0.0387
Total	0.4776	0.7714

6.4. Experimental test results

The experimental platform is configured with the proposed EHGO-RLS-DI. In this case, a second order EHGO is utilized. The control gains for the plant and reference system are $k_{x_1} = k_{y_1} = 4$, $k_{z_1} = 5$, $k_{x_2} = k_{y_2} = 5$, $k_{z_2} = 7.5$, $k_1 = 2$, and $k_2 = 4$. The control parameters are chosen as $\varepsilon_1 = 0.18$, $\varepsilon_2 = 0.0013$, $\varepsilon_3 = 0.0012$, which satisfy (17). The initial condition of P_0 in (7) is chosen as $P_0 = 0.18 \cdot I_3$. The EHGO gains defined in (4) are $\alpha_{i2} = 0.074$, $\alpha_{i3} = 0.0001$, $\alpha_{j2} = 0.166$, $\alpha_{j3} = 0.0001$.

The objective of the experiment is to track the reference trajectories X_r and ψ_r in the presence of disturbances and uncertainties. To fulfill the condition, we conducted the outdoor experiment under strong wind gust conditions with an average wind speed of 3.2 (m/s) according to the weather report. Note that the wind gust is the main source of the external disturbances σ_X and σ_Θ, and it is well-assumed to be continuously differentiable. In addition, we can assume that the speed of the wind gust is bounded since it has a finite power of disturbances. We conducted the experimental test as follows. Initially, the quadrotor was flown by a remote control transmitter. Once the quadrotor was stabilized, the trajectory tracking mode was activated. The trajectory tracking mode includes three consecutive tasks; position-holding mode, circle-tracking mode, and again position-holding mode. For $0 \le t < 15$, the position-holding mode is activated with reference trajectories $x_r = x_{init}$, $y_r = y_{init}$, $z_r = z_{init}$, and $\psi_r = 0$ where subscript $init$ indicates the initial positions. Then, for $15 \le t < 55$, the circle-tracking mode is activated with reference trajectories $x_r = x_{init} + 2.5 \cdot \cos(\pi t/10)$, $y_r = y_{init} + 2.5 \cdot \sin(\pi t/10)$, $z_r = z_{init}$, and $\psi_r = 0$. Lastly, for $t \ge 55$, the quadrotor holds its position on the initial positions, $x_r = x_{init}$, $y_r = y_{init}$, $z_r = z_{init}$, and $\psi_r = 0$. The tasked reference trajectory is shown in Fig. 6.

In Fig. 6, the hardware experiment results of the EHGO-RLS-DI and EHGO-FL are presented. Utilizing EHGO, both methods were able to track trajectories under external disturbances, which are primarily due to wind gusts. Before the activation of the trajectory tracking mode, the quadrotor moved freely in both the x and y directions. After the activation, the quadrotor attempted to move to the location where the mode was activated. Then the quadrotor tracked the given trajectories smoothly. In Table 2, the RMSe values are introduced to present the superior performance of the EHGO-RLS-DI over the EHGO-FL. The result shows that the EHGO-RLS-DI improves the RMSe value over the EHGO-FL by 44.5%, 29.7%, 36.4%, 44%, and 38.1% for x, y, z, ψ, and as a total, respectively. The frame-by-frame time-lapse images of the outdoor hardware experiments are shown in Fig. 7. The video of the outdoor experiment can also be found in the following link: https://youtu.be/ltcx1X3WuIU.

7. Conclusions

In this paper, we developed a novel trajectory tracking output feedback control design for quadrotors in the presence of uncertainties and disturbances using the recursive least square method with dynamic inversion (RLS-DI). The multi-time-scale approach was well suited to this problem to deal with the underactuation present in quadrotors. The FL for the translational dynamics was in charge of resolving non-affine control inputs, whereas the dynamic inversion based on the recursive least square method for the rotational dynamics dealt with uncertain input coefficients. The EHGO provides estimates of unmeasurable system

states and uncertainties for the controllers. We presented the comprehensive stability analysis of the closed-loop system using the singular perturbation method. Through numerical simulation, we showed that our proposed control EHGO-RLS-DI is suitable to attenuate the disturbances and uncertainties in the input Jacobian, and it outperforms the EHGO-FL and DOB-CSMC control method. Furthermore, the outdoor experiments in the wind gusts showed that our EHGO-RLS-DI overcame the disturbances and successfully tracked the reference trajectories, and outperformed the EHGO-FL.

CRediT authorship contribution statement

Seongwon Lee: Conceptualization, Methodology, Software, Investigation, Writing – original draft. **Joowhan Seo:** Software, Visualization, Investigation, Writing – review & editing. **Joonho Lee:** Formal analysis, Supervision, Project administration, Writing – review & editing. **Connor Boss:** Resources, Writing – review & editing. **Jongeun Choi:** Supervision, Funding acquisition, Writing - Review & Editing.

Declaration of competing interest

The authors declare the following financial interests/personal relationships which may be considered as potential competing interests: Jongeun Choi reports financial support was provided by National Research Foundation of Korea.

Data availability

No data was used for the research described in the article.

Acknowledgments

This work was supported by the National Research Foundation of Korea (NRF), South Korea grant funded by the Korea government (MSIT). (No. 2021R1A2B5B01002620)

References

[1] Castillo P, Lozano R, Dzul A. Stabilization of a mini-rotorcraft having four rotors. In: IEEE/RSJ int. conf. intell. robots syst., Vol. 3. IROS, IEEE; 2004, p. 2693–8.
[2] Herrera M, Chamorro W, Gómez AP, Camacho O. Sliding mode control: An approach to control a quadrotor. In: Asia-pacific conf. comput. aided syst. eng.. IEEE; 2015, p. 314–9.
[3] Lu B, Fang Y, Sun N. Continuous sliding mode control strategy for a class of nonlinear underactuated system. IEEE Trans Automat Control 2018;63(10):3471–8.
[4] Fang X, Shang Y. Trajectory tracking control for small-scale unmanned helicopters with mismatched disturbances based on a continuous sliding mode approach. Int J Aerosp Eng 2019;2019.
[5] Choi I-H, Bang H-C. Adaptive command filtered backstepping tracking controller design for quadrotor unmanned aerial vehicle. Proc Inst Mech Eng G 2012;226(5):483–97.
[6] Jiang T, Lin D, Song T. Finite-time backstepping control for quadrotors with disturbances and input constraints. IEEE Access 2018;6:62037–49.
[7] Wang N, Su S-F, Han M, Chen W-H. Backpropagating constraints-based trajectory tracking control of a quadrotor with constrained actuator dynamics and complex unknowns. IEEE Trans Syst Man Cybern: Syst 2018;49(7):1322–37.
[8] Wang N, Ahn CK. Coordinated trajectory-tracking control of a marine aerial-surface heterogeneous system. IEEE/ASME Trans Mechatronics 2021;26(6):3198–210.
[9] Zhao B, Xian B, Zhang Y, Zhang X. Nonlinear robust adaptive tracking control of a quadrotor UAV via immersion and invariance methodology. IEEE Trans Ind Electron 2014;62(5):2891–902.
[10] Raffo GV, Ortega MG, Rubio FR. An integral predictive/nonlinear H8 control structure for a quadrotor helicopter. Automatica 2010;46(1):29–39.
[11] Geiser M, Xargay E, Hovakimyan N, Bierling T, Holzapfel F. L1 adaptive augmented dynamic inversion controller for a high agility UAV. In: AIAA guid. navig. control conf.. 2011, p. 6457.
[12] Xiao B, Yin S. A new disturbance attenuation control scheme for quadrotor unmanned aerial vehicles. IEEE Trans Ind Inf 2017;13(6):2922–32.
[13] Ma H-J, Liu Y, Li T, Yang G-H. Nonlinear high-gain observer-based diagnosis and compensation for actuator and sensor faults in a quadrotor unmanned aerial vehicle. IEEE Trans Ind Inf 2018;15(1):550–62.
[14] Liu Z, Liu X, Chen J, Fang C. Altitude control for variable load quadrotor via learning rate based robust sliding mode controller. IEEE Access 2019;7:9736–44.
[15] Qiao J, Liu Z, Zhang Y. Payload dropping control of an unmanned quadrotor helicopter based on backstepping controller. In: MATEC web of conferences, Vol. 277. EDP Sciences; 2019, p. 01004.
[16] Dierks T, Jagannathan S. Output feedback control of a quadrotor UAV using neural networks. IEEE Trans Neural Netw 2009;21(1):50–66.
[17] Shi G, Shi X, O'Connell M, Yu R, Azizzadenesheli K, Anandkumar A, Yue Y, Chung S-J. Neural lander: Stable drone landing control using learned dynamics. In: Int. conf. rob. autom.. ICRA, IEEE; 2019, p. 9784–90.
[18] Bisheban M, Lee T. Geometric adaptive control with neural networks for a quadrotor UAV in wind fields. 2019, arXiv arXiv–1903.
[19] Lopez-Sanchez I, Moyrón J, Moreno-Valenzuela J. Adaptive neural network-based trajectory tracking outer loop control for a quadrotor. Aerosp Sci Technol 2022;129:107847.
[20] Seo J, Lee S, Lee J, Choi J. Nonaffine helicopter control design and implementation based on a robust explicit nonlinear model predictive control. IEEE Trans Control Syst Technol 2021;accepted.
[21] Lee J, Mukherjee R, Khalil HK. Output feedback stabilization of inverted pendulum on a cart in the presence of uncertainties. Automatica 2015;54:146–57.
[22] Lee J. Output feedback control in the presence of uncertainties: Using extended high-gain observers with dynamic inversion. Michigan State University; 2014.
[23] Khalil HK, Grizzle JW. Nonlinear system, Vol. 3. Upper Saddle River, NJ: Prentice hall; 2002.
[24] Freidovich LB, Khalil HK. Performance recovery of feedback-linearization-based designs. IEEE Trans Automat Control 2008;53(10):2324–34.
[25] Benallegue A, Mokhtari A, Fridman L. High-order sliding-mode observer for a quadrotor UAV. Internat J Robust Nonlinear Control 2008;18(4–5):427–40.
[26] Marconi L, Naldi R. Robust full degree-of-freedom tracking control of a helicopter. Automatica 2007;43(11):1909–20.
[27] Marconi L, Naldi R. Aggressive control of helicopters in presence of parametric and dynamical uncertainties. Mechatronics 2008;18(7):381–9.
[28] Khalil H. Nonlinear systems, Vol. 3. Prentice hall; 2002.
[29] Rouche N, Habets P, Laloy M. Stability theory by Liapunov's direct method, Vol. 4. Springer; 1977.
[30] Fum WZ. Implementation of Simulink controller design on Iris+ quadrotor. Tech. rep., Monterey United States: Naval Postgraduate School; 2015.

Seongwon Lee received his B.S. degree in Mechanical Engineering from Yonsei University at Seoul, South Korea in 2021. He is now pursuing his Ph.D. degree in Department of Mechanical Science and Engineering at University of Illinois Urbana-Champaign. His research interests include task and motion planning, deep reinforcement learning, autonomous driving, and nonlinear control with applications to unmanned aerial vehicles (UAV), ground vehicles, and manipulators.

Joohwan Seo received his B.S. degree in Mechanical engineering from Yonsei University at Seoul, South Korea in 2019, where he is currently pursuing the M.S. degree. He worked in Machine Learning and Control Systems (MLCS) Laboratory. Now he is pursuing his Ph.D. degree in Department of Mechanical Engineering at University of California, Berkeley. His research interests include nonlinear control, learning-based control, and reinforcement learning, with applications to unmanned aerial vehicles (UAV) and robots.

Joonho Lee received the B.S. degree from Dong-a University, Busan, South Korea in 2004, the M.S. degree from Yonsei University, Seoul, South Korea in 2006, and the Ph.D. degree from Michigan State University, East Lansing in 2015, all in mechanical engineering. In 2015, he was a Research Associate in the Department of Mechanical Engineering at Michigan State University to design and implement control algorithms for autonomous vehicles in the presence of uncertainties. From 2016, he moved to the Department of Mechanical Engineering at Cleveland State University, where he conducted research on a powered prosthetic leg and cyber-enabled machine as a Research Associate. He was working on control design for autonomous cars at HRL Laboratories, LLC (formerly Hughes Research Laboratories). From 2018 to March, 2022, he worked for General Motors, R&D. At General Motors, R&D he was working on wheel control algorithms such as Traction Controls and Engine Drag using Explicit Nonlinear

Model Predictive Control (ENMPC). In addition, he conducted research on deep reinforcement learning based on a multi time-scale structure and stochastic approximation (e.g., the ODE method) for the applications to ground vehicles. Currently, he is a Sr. Engineer for Guidance Navigation Controls & Autonomy at Boeing Research and Technology. His research interests include the areas of Deep Reinforcement Learning based Stochastic Approximation, nonlinear controls, specifically a multi-time-scale approach, estimators designs (Graph Neural Networks, Machine Learning, conventional observers), under-actuated mechanical systems (vehicle chassis and wheels dynamics, helicopters, quadrotors, etc.).

Connor J. Boss received his B.S. and Ph.D. degrees in electrical engineering from Michigan State University in 2015 and 2021, respectively. He is currently Senior Professional Staff in the Space Exploration Sector at The Johns Hopkins University Applied Physics Laboratory. His research interests include the development and analysis of control systems, embedded system development, and the control of multi-rotor unmanned aerial vehicles. His past research experience includes system identification and modeling of human motor control.

Jongeun Choi received the B.S. degree in mechanical design and production engineering from Yonsei University, Seoul, South Korea, in 1998, and the M.S. and Ph.D. degrees in mechanical engineering from the University of California at Berkeley, in 2002 and 2006, respectively. He is a visiting scholar at UC Berkeley in 2023 and a Professor with the School of Mechanical Engineering, Yonsei University. From 2020 to 2022, he served as the Graduate Program Chair of the School of Mechanical Engineering, Yonsei University. During 2019-2023, he served the Chairperson of the Department of Vehicle Convergence Engineering, Yonsei University, funded by Hyundai Motor Company. From 2020, he is affiliated with the Department of Artificial Intelligence, Yonsei University. Prior to joining Yonsei University, he worked for ten years as an Associate Professor (2012-2016) and an Assistant Professor (2006-2012), with the Department of Mechanical Engineering, and also with the Department of Electrical and Computer Engineering, Michigan State University. His current research interests include machine learning, systems and control, deep reinforcement learning, and Bayesian methods with applications to robotics, self-driving vehicles, and medical machine learning.

He serves as a Senior Editor of the International Journal of Control, Automation, and Systems (IJCAS) from 2023. He also served as a Guest Editor with a two-year term (2021-2022) for the IEEE/ASME TMECH/AIM Focused Section on Emerging Topics. He co-organized and co-edited special issues on Stochastic Models, Control, and Algorithms in Robotics in Journal of Dynamic Systems, Measurement and Control (JDSMC), from 2014 to 2015. He served as an Associate Editor for the IEEE Robotics and Automation letters (RA-L), in 2018, Journal of Dynamic Systems, Measurement and Control (JDSMC) during 2014-2019, and International Journal of Precision Engineering and Manufacturing (IJPEM) during 2017-2018. He served as a Senior Editor for Ubiquitous Robots (UR), in 2020 and as an Associate Editor for 2021 IEEE International Conference on Robotics and Automation (ICRA).

He received the Best Conference Paper Award at the 12th International Conference on Ubiquitous Robots and Ambient Intelligence (URAI), in 2015. His articles were finalists for the Best Student Paper Award at the 24th American Control Conference (ACC), in 2005, and the Dynamic System and Control Conference (DSCC), in 2011 and 2012. He was a recipient of an NSF CAREER Award, in 2009. He is a member of ASME and IEEE.